

# Multi-scale Modeling of Oxygen Vacancies Assisted Charge Transport in Sub-Stoichiometric $\text{TiO}_x$ For RRAM Application

O. Pirrotta, A. Padovani, L. Larcher

DISMI - Department of Science and Methods for Engineering  
University of Modena and Reggio Emilia  
Reggio Emilia, Italy  
Email: onofrio.pirrotta@unimore.it

L. Zhao, B. Magyari-Köpe, Y. Nishi

Stanford University Group  
Stanford University  
Stanford, CA, USA  
Email: lzhao10@stanford.edu

**Abstract**—In this work we investigate the charge transport in sub-stoichiometric  $\text{TiO}_x$  for RRAM applications. We explored the atomic defect configurations actively assisting the charge transport in sub-stoichiometric  $\text{TiO}_x$  through a multi-scale approach. We combined density-functional-theory-based non-equilibrium Green's function approach (DFT-NEGF) with physical-based trap assisted tunneling (TAT) modeling to identify the defects dominating the current conduction mechanism and the physical parameters of the defects responsible for the trap-assisted tunneling (TAT). The values of the thermal ionization energy  $E_T$  and relaxation energy  $E_{REL}$  extracted are 0.35-0.4eV and 0.7eV, respectively.

**Keywords**—Trap Assisted Tunneling, Marcus theory, DFT, NEGF,  $\text{TiO}_x$ , RRAM

## I. INTRODUCTION

The interest on resistive random access memories (RRAM) has increased significantly in the last years, because of their potentials as emerging non-volatile memory technologies [1-3]. Among the variety of materials proposed,  $\text{TiO}_2$  is very promising because of the reliable resistive switching and compatibility with the CMOS process [4,5].

Nevertheless, a complete understanding of the physical mechanisms governing the  $\text{TiO}_2$  RRAM operations (i.e. forming and resistive switching) and the charge transport in different resistive states is lacking. In particular, the understanding of the dependence of the charge transport on the oxygen vacancy concentration and temperature in the  $\text{TiO}_x$  film needs to be investigated to correlate the current to the atomistic characteristics of the material.

In this scenario, the aim of this work is to investigate the atomic defect configurations actively assisting the charge transport in sub-stoichiometric  $\text{TiO}_x$ , and to discuss the physical mechanism governing the charge transport at different  $\text{TiO}_x$  stoichiometry levels, corresponding to the conductive filament conditions in different RRAM operation regimes, i.e., before forming, Low-Resistance-State (LRS) and High-Resistance State (HRS). To this purpose, we use a multi-scale simulation methodology that combines density-functional-theory-based non-equilibrium Green's function approach (DFT-NEGF), used to calculate the coherent electron transport, with the multiphonon trap-assisted tunneling (TAT) model, to incorporate the electron-phonon coupling and lattice relaxation. The current-voltage characteristics from both origins are simulated and compared at various levels of oxygen deficiency. This multi-scale approach provides a comprehensive picture of electron transport from the atomistic level, allowing gaining insights into different regimes of filament conductivity in TMO-based RRAM.

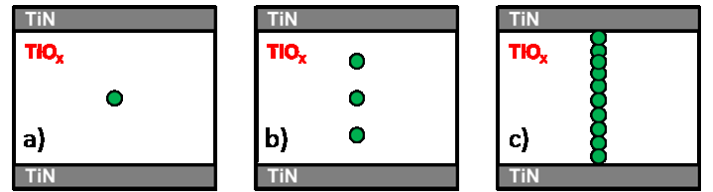


Fig. 1 Schematic illustration of the simulated stacks: a) single isolated defect ( $1V_o$ ); b) 3 defects equally spaced along the oxide thickness ( $3V_o$ ); c) conductive filament (CF) ( $9V_o$ ).

## II. DEVICES AND MULTI-SCALE SIMULATION METHODOLOGY

In this study we considered a  $\text{TiN}/\text{TiO}_x/\text{TiN}$  MIM capacitor system with 3nm-thick  $\text{TiO}_x$ . A multi-scale approach is applied to investigate the atomic defect configurations responsible for charge transport in  $\text{TiO}_x$ . To account for the vacancy-vacancy interaction and its impact on the transport-related properties in different resistive states, we consider different scenarios shown in Fig. 1: a) one isolated O vacancy defect ( $1V_o$ ) in the middle of the dielectric layer; b) 3 equally spaced O vacancies ( $3V_o$ ) along the dielectric thickness; c) 9 equally spaced  $V_o$  ( $9V_o$ , 3Å between each other), mimicking the ohmic-like conductive filament in Low Resistive State (LRS), i.e. after forming.

In the DFT-NEGF approach, the device configurations corresponding to these scenarios (Fig. 2) are first created by matching cubic TiN lattices to unstressed rutile  $\text{TiO}_2$ , with the tensile strain optimized to 3% in both X and Y directions. The supercell size is roughly  $0.9 \times 0.9 \times 4.0$  nm, with a total 316 atoms minus the number of  $V_o$ . The atomic positions are relaxed using LDA+U with PAW [6], implemented by the Vienna Ab-initio Simulation Package (VASP) [7].

The relaxed configurations are then brought to QuantumWise ATK software [8] for DFT-based quantum transport calculations. The voltage drop across the device is varied from 0.1V to 0.75V, and  $8 \times 8 \times 1$  Monkhorst-Pack k-mesh is applied to calculate the transmission.

The electron-phonon coupling effect on the charge-transport is included through the multiphonon TAT model [9], [10], which accounts for the lattice relaxation associated with carrier capture and emission at O vacancy defects along the conductive path. The modification in the defect atomic structure upon charge trapping and emission is described by the multi-phonon transition probability calculated in the framework of the non-adiabatic non-radiative interaction [9], [10]. The reduction of the relaxation energy,  $E_{REL}$ , at increasingly level of O deficiency is modeled according to the Marcus theory, which describes the electron transfer in chemical reactions [11].

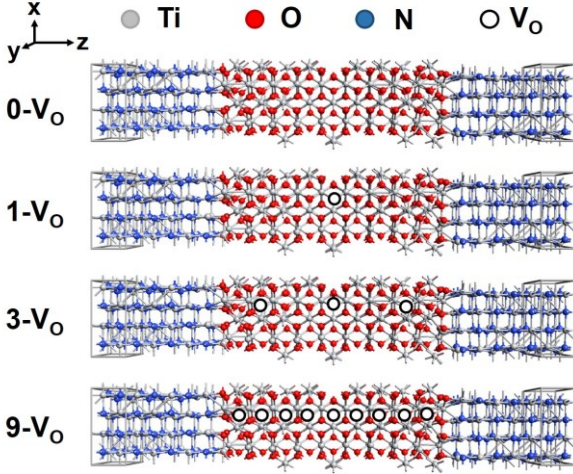


**Fig. 2** Atomic arrangements of the TiN/TiO<sub>2</sub>/TiN device structures used in the DFT simulations, with 1,3 and 9 V<sub>O</sub> in TiO<sub>2</sub>. The device structure with no V<sub>O</sub> in TiO<sub>2</sub> (0 V<sub>O</sub>) is computed as a reference, which accounts for the direct tunneling effects.

This reduction is due to the increased coupling between electrons trapped at adjacent O vacancy defects when their distance  $d$  reduces below a certain value. Figure 3 shows the configuration diagrams for the electron transfer in two conditions: a) large  $d$ , no coupling between adjacent electron states; b) short  $d$ , the coupling between adjacent defects reduces the relaxation  $E_{REL}$ , and activation energy,  $E_{act}$ .

In the a) case, the electron involved in the charge transfer is localized at defect/donor sites. No coupling occurs between the electron states localized at initial and final defect states, and the charge transfer can be described in the framework of the multiphonon TAT theory [9], [10]. In the b) case, the coupling between electrons trapped at adjacent defect sites reduces the relaxation energy because of the energy level splitting. The relaxation/self-organization energy, which results in the decrease of the activation energy, can be calculated as:

$$E_{REL}(d) = S\hbar\omega + \left(\frac{1}{r} - \frac{1}{d}\right) \cdot \left(\frac{1}{\epsilon_{op}} - \frac{1}{\epsilon_s}\right) \cdot \frac{\Delta e^2}{4\pi\epsilon_0} \quad (1)$$

where  $S$  is the Huang-Rhys factor which represents the number of phonons required for the atomic-scale lattice rearrangement around the defect needed to accommodate the trapped charge [12];  $\hbar\omega$  is the effective energy of the phonons associated with the charge trapping/emission mechanisms;  $r \approx 3\text{\AA}$  is the radius of the defect capture cross section;  $\epsilon_{op}=7$  and  $\epsilon_s=85$  are the optical and static dielectric constants of TiO<sub>2</sub> [13], respectively;  $\epsilon_0$  is the vacuum permittivity and  $\Delta e=1e$  is the amount of charge transferred.

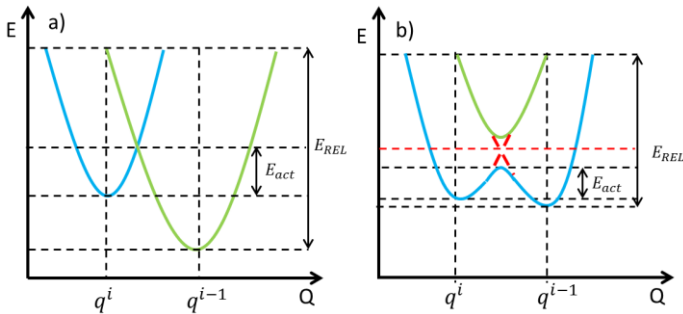


**Fig. 3.** Illustration of the energy configuration diagram for electron transmission according to Marcus theory: a) large distance  $d$  between the defects results in no electronic coupling, and nominal relaxation,  $E_{REL}$ , and activation energy  $E_{act}$ ; b) at short distance, the coupling between trapped electron states in adjacent defects, reduces both  $E_{REL}$  and  $E_{act}$ .

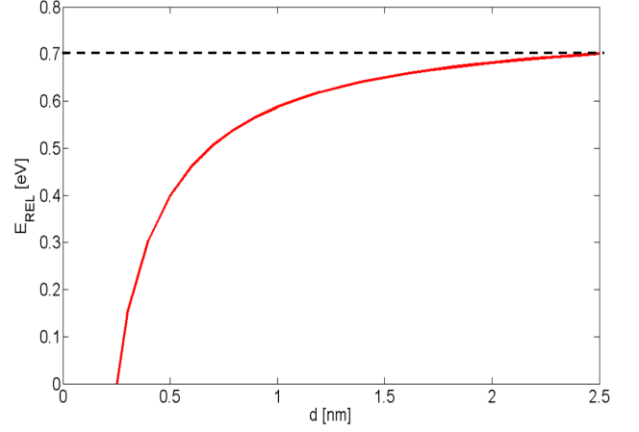


**Fig. 4.** Relaxation energy  $E_{REL}$  vs the distance between O vacancies,  $d$ . The horizontal dashed line indicates the relaxation energy value of 0.7eV calculated using DFT method for isolated oxygen vacancies.

Figure 4 shows  $E_{REL}$  as a function of the distance between O vacancy defects: the relaxation energy reduces with the distance between traps, dropping to zero at  $d \sim 2.5\text{-}3\text{\AA}$ , which corresponds to the conditions in which a sub-band is created by the high defect density [14]. In this condition, the conduction mechanism passes from TAT to drift, and the conductivity of the filament is calculated according to the Landauer formalism [15].

The physical parameters (i.e. thermal ionization,  $E_T$ , and relaxation energies) of the O vacancy defects in different charge states are calculated with LDA+U method using a  $3 \times 3 \times 4$  supercell of rutile TiO<sub>2</sub> with a total of 216 atoms obtained with VASP. Based on previous results the positively-charged oxygen vacancies ( $V^+$ ) are identified as the defects assisting the charge transport in these devices [9, 10, 16]. The TAT current is calculated by MDLab package [17].

The TAT current driven through a given conductive path  $I_{path}$  (i.e. 1Vo, 3Vo and 9Vo, see Fig 1) is determined by the slowest trap along the path through

$$I_{path} = q / \max_j(\tau_{c,j} + \tau_{e,j}), \quad (2)$$

where  $q$  is the electron charge;  $\tau_{c,j}$  and  $\tau_{e,j}$  are the time constants of electron capture and emission associated with the  $j^{\text{th}}$  traps in the conductive path, respectively [9, 18].  $\tau_{c,j}$  and  $\tau_{e,j}$  are calculated by taking into account the electron-phonon coupling and the lattice relaxation associated with charge capture and emission process [12, 19].

The defect characteristics match those of positively charged oxygen vacancies, calculated by density-functional-theory-based non-equilibrium Green's function approach (DFT-NEGF) techniques.

### III. RESULTS AND DISCUSSION

Figure 5 shows the current-voltage characteristics calculated for the four device configurations using NEGF. Non-linear I-V characteristics were observed for the 0-V<sub>O</sub>, 1-V<sub>O</sub> and 3-V<sub>O</sub> configurations, which suggests the conduction mechanism to be direct tunneling (0-V<sub>O</sub>) or trap-assisted tunneling (1-V<sub>O</sub>, 3-V<sub>O</sub>). In the 9-V<sub>O</sub> case, on the other hand, the I-V characteristic is linear, indicating quasi-metallic conduction.

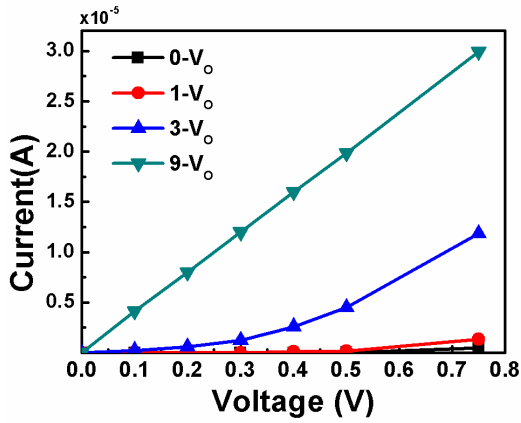
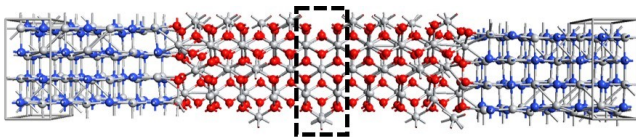


Fig. 5 I-V characteristics for the device configurations shown in Fig. 2.

To further understand the electronic structures of the defect configurations, the site-projected DOS in the central region of the device are calculated and summed up, as shown in Figure 6. In all cases, only one oxygen vacancy is contained in the DOS-summation region (represented by the dashed frame in Fig. 6). In the 0- $V_O$  case, no defect state is observed within the bandgap. In the 1- $V_O$  and 3- $V_O$  cases, one defect level is observed within the bandgap, indicating isolated vacancy and weak  $V_O$ - $V_O$  interactions. In the 9- $V_O$  case, a series of defect levels are observed on a large portion of the bandgap. This implies strong interactions between  $V_O$  and good conductivity due to abundant states near the Fermi level.



The site-projected DOS of the atoms in the dashed frame are added up and plotted below

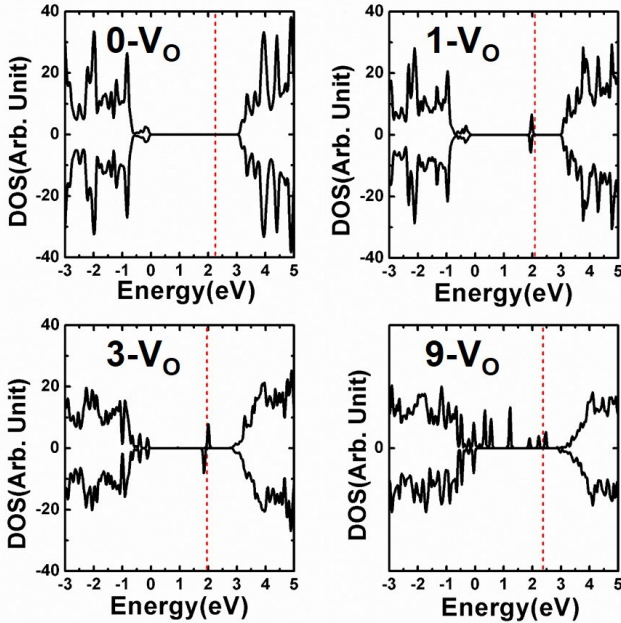


Fig. 6 Summation of site projected DOS in the central region of the device, for the device configurations shown in Fig. 2.

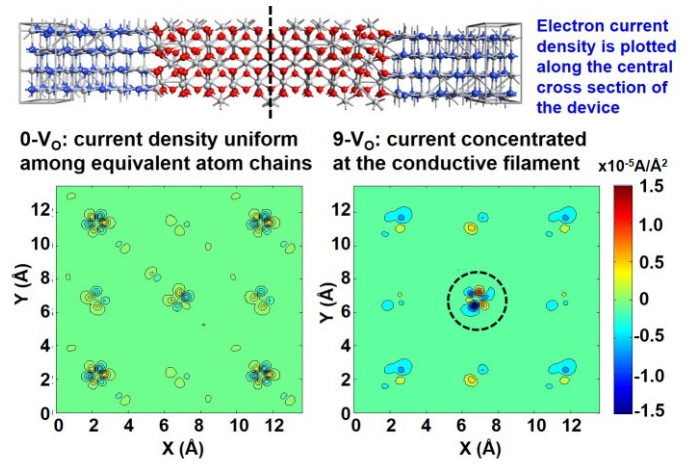


Fig. 7 Comparison of the current-density distributions along the central cross section of the 0- $V_O$  configuration and the 9- $V_O$  configuration as shown in Fig. 2.

The spatial distribution of current densities in the regimes of tunneling (0- $V_O$ ) and metallic conduction (9- $V_O$ ) are further studied and compared, as shown in Fig. 7. In the case of 0- $V_O$ , the current densities are evenly distributed near equivalent atomic chains. While for the 9- $V_O$  configuration, the conduction current is largely concentrated around the  $V_O$  chain, which confirms the filament as the origin of metallic conduction.

These results are consistent with reported experimental observations of dielectric breakdown and resistive switching mechanism in  $TiO_2$  stacks [4]. Since the current calculated through the DFT-NEGF approach does not include contributions from the electron-phonon coupling at  $V_O$  defects, here we consider these contributions from current simulations performed through the multi-phonon TAT model included in the MDLab simulation package [9, 10, 16, 17]. For these simulations, we considered for isolated  $V_O$  defects the values for thermal ionization ( $E_I=0.35-0.4eV$ ) and relaxation ( $E_{REL}=0.7eV$ ) energies extracted from DFT calculations, which are associated with positively charged oxygen vacancies, previously identified as the defect species responsible for the charge transport in  $TiO_x$  at different levels of sub-stoichiometry [9, 10, 16].

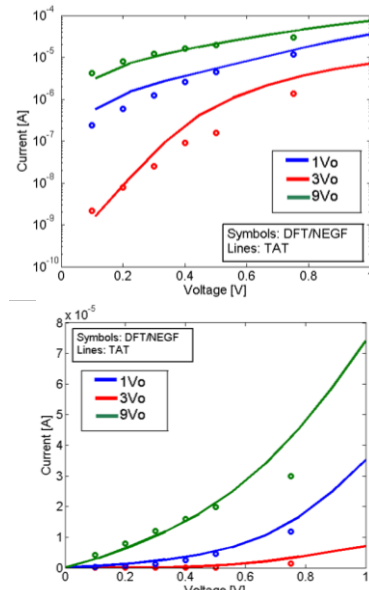
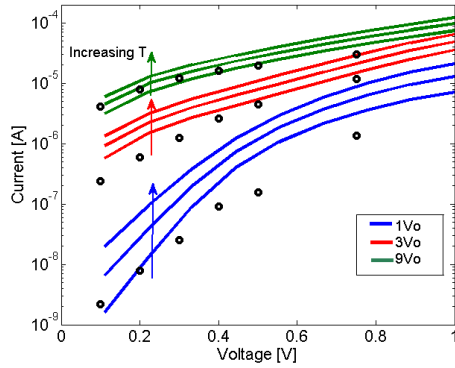


Fig. 8. Current-voltage characteristics simulated for the three defects configuration (i.e., 1 $V_O$ , 3 $V_O$ , and 9 $V_O$ ) with TAT (lines) and DFT/NEGF (symbols) models, plotted in logarithmic and linear fashion in the upper and lower figures, respectively.



**Fig. 9.** Current-voltage characteristics simulated at different temperatures (i.e. 25°C, 75°C and 125°C) for the 1Vo, 3Vo, 9Vo defect configurations using the TAT (solid lines) and DFT/NEGF (symbols) models.

The currents simulated by including electron-phonon coupling and lattice relaxation are higher by a factor of  $\sim 5$  (3) in the 1-V0 (3-V0) case than those accounting only for the coherent processes. The wider difference between coherent and TAT calculations occurs around  $\sim 0.5V$ , where the electron-trap interaction effect on the current (which depends on the thermal ionization and relaxation energy of defects [9]) is maximum. Compared to similar study reported in the literature [6], the current increase is lower because of the relatively low conduction band offset between TiN and TiO<sub>2</sub>.

The TAT simulations allow also describing the temperature dependency of the current, which is related to the lattice relaxation accompanying charge trapping and emission processes. The current-voltage characteristics calculated at different temperatures (i.e. 25°C, 75°C and 125°C) with the TAT model are shown in Fig. 9. No temperature dependence is shown on the I-V characteristics calculated using the NEGF approach, as the only temperature dependent effect included in this case (which is indeed negligible) is the increase in the electrons energy distribution.

The activation energy of TAT current simulations,  $E_{act}$ , is extracted from the Arrhenius plot of the I-V curves simulated for different defect configurations, Fig. 10.  $E_{act}$  reduces at higher O deficiency because of the increased coupling between electrons trapped at adjacent defect sites, which lowers the relaxation and the activation energy. The inclusion of the electron-phonon coupling effect results thus to be of primary importance to fully describe the operation of RRAM these devices.

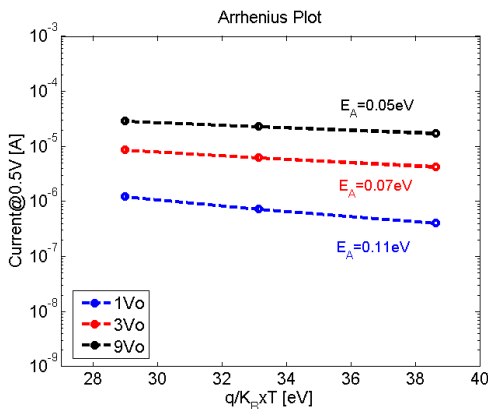


**Fig. 10.** Activation energy extracted for the I-V curves simulated using the TAT model on the TiO<sub>2</sub> stacks: the activation energy reduces at higher O deficiency.

#### IV. CONCLUSIONS

We presented a multi-scale modeling approach to simulate charge transport assisted by oxygen vacancy defects in sub-stoichiometric TiO<sub>x</sub>. The positively charged O vacancy are identified as the defects dominating the charge transport, and the role of electron-phonon coupling and lattice relaxation appear crucial to describe the magnitude and the temperature dependency of the current.

#### ACKNOWLEDGMENTS

This work is partially supported by Stanford non-volatile memory research initiative (NMTRI). The DFT and NEGF calculations are partly carried out at NNIN Computing Facility of Stanford University. This work also used the Extreme Science and Engineering Discovery Environment (XSEDE) which is supported by National Science Foundation grant number ACI-1053575, and the Center for Nanoscale Materials which is supported by the U. S. Department of Energy, under Contract No. DE-AC02-06CH11357.

#### REFERENCES

- [1] H.-S. P. Wong *et al.*, Proc. of the IEEE, vol. 100, No. 6, pp. 1951-1970, June, 2012.
- [2] B. Magyari-Köpe *et al.*, Nanotechnology 22, no 25, p. 254029, 2011.
- [3] G. Bersuker *et al.*, J. of Appl. Phys., vol. 110, p. 124518, December 2011.
- [4] D. Acharyya *et al.*, Microel. Rel. 54, pp.541-560, 2014.
- [5] D.-H. Kwon *et al.*, Nature Nanotech. vol. 5, pp. 148, 2010..
- [6] S.G. Park, *et al.*, Phys. Rev. B vol. 82, pp. 115109,2010.
- [7] G. Kresse *et al.*, Phys. Rev. B, vol. 47, pp. 558, 1993.
- [8] Atomistix ToolKit, QuantumWise A/S (www.quantumwise.com).
- [9] L. Vandelli *et al.*, IEEE Trans. Electron Devices, vol. 58, no. 9, pp. 2878-2887, September 2011.
- [10] A. Padovani *et al.*, IEEE Electron Device Lett., vol. 34, no. 5, pp. 680-682, May 2013.
- [11] Rudolph A. Marcus, Rev. Mod. Physics, vol 65, pp. 599-610, July 1993.
- [12] K. Huang and A. Rhys, Proc. R. Soc. London, Ser. A 204, 406, 1950.
- [13] J. Robertson, Rep. Prog. Phys. 69, pp. 327-396, 2006.
- [14] G. Bersuker *et al.*, JAP 110, 124518, 2011
- [15] R. Landauer, IBM Journal of Research and Development ,vol. 1, pp. 223-231, 1957.
- [16] L. Larcher *et al.*, Journal of Computational Electronics, vol. 12, no. 4, pp. 658-665, December 2013.
- [17] www.mdlab-software.com
- [18] L. Larcher, IEEE Trans. Electron Devices 50, 1246 (2003).
- [19] M. Hermann and A. Schenk, J. Appl. Phys. 77, 4522 (1995).